

Quantifying Oil-Recovery Mechanisms during Natural-Gas Huff 'n' Puff Experiments on Ultratight Core Plugs

Son Tran, Mahmood Reza Yassin, Sara Eghbali, Mohammad Hossein Doranegard,
and Hassan Dehghanpour*, University of Alberta

Summary

Despite promising natural gas huff 'n' puff (HnP) field-pilot results, the dominant oil-recovery mechanisms during this process are poorly understood. We conduct systematic natural-gas (C_1 and a mixture of C_1/C_2 with the molar ratio of 70:30) HnP experiments on an ultratight core plug collected from the Montney tight-oil formation, under reservoir conditions ($P = 137.9$ bar and $T = 50^\circ\text{C}$). We used a custom-designed visualization cell to experimentally evaluate mechanisms controlling gas transport into the plug during injection and soaking phases and oil recovery during the whole process. The tests also allow us to investigate effects of gas composition and initial differential pressure between injected gas and the plug ($\Delta P_i = P_g - P_o$) on the gas-transport and oil-recovery mechanisms. Moreover, we performed a Pécelt number, N_{Pe} , analysis to quantify the contribution of each transport mechanism during the soaking period.

We found that advective-dominated transport is the mechanism responsible for the transport of gas into the plug at early times of the soaking period ($N_{Pe} = 1.58$ to 3.03). When the soaking progresses, N_{Pe} ranges from 0.26 to 0.62, indicating the dominance of molecular diffusion. The advective flow caused by ΔP_i during gas injection and soaking leads to improved gas transport into the plug. Total system compressibility, oil swelling, and vaporization of oil components into the gas phase are the recovery mechanisms observed during gas injection and soaking, while gas expansion is the main mechanism during depressurization phase. Overall, gas expansion is the dominant mechanism, followed by total system compressibility, oil swelling, and vaporization. During the "puff" period, the expansion and flow of diffused gas drag the oil along its flowpaths, resulting in a significant flow of oil and gas observed on the surface of the plug. The enrichment of injected gas by 30-mol% C_2 enhances the transport of gas into the plug and increases oil recovery compared to pure C_1 cases.

Introduction

Oil production from tight reservoirs has quickly grown to offset the rapid decline of conventional oil production. Tight oil is defined as oil trapped in low-permeability shale, sandstone, and carbonate formations that accounted for 59% of total US crude oil production in 2018 (EIA 2019). According to Nelson (2009) and Ma and Holditch (2015), the rock matrix in tight reservoirs typically has permeability and porosity of less than 0.1 md and 10%, respectively.

The Montney Formation in the Western Canadian Sedimentary Basin is a world-class unconventional petroleum resource with the oil in place of 141×10^9 barrels (Canada Energy Regulator 2013). The unconventional portion of this formation consists of mainly siltstone interbedded with thin shales, variable amounts of sandstone, and has a thickness ranging from 100 to 300 m (Reynolds et al. 2015). The gas permeability (by the pulse-decay technique) of rock samples collected across the formation varies from 0.1 to 2×10^{-5} md (Ghanizadeh et al. 2015).

Advances in multistage hydraulic fracturing and horizontal drilling technologies have led to a substantial increase in tight-oil production. However, rapid decline rates and low oil recovery factors (typically less than 10% of initial oil in place) after primary production are key challenges for sustainable development of such formations (Hughes 2013; King 2014; Gherabati et al. 2017). These challenges turn out to be an incentive for enhanced oil recovery (EOR) investments. There has been a growing interest in using associated gases for gas-injection EOR and reducing gas flaring (Hoffman and Evans 2016; Jin et al. 2017). The enrichment of injected gas, for example, by adding carbon dioxide (CO_2) and/or light hydrocarbon components, improves the miscibility of the gas/oil system. With the rapid growth in shale oil/gas production, C_2 has been available at a less-expensive price than propane and butane (McGuire et al. 2017). The conventional gas-injection approach using well pairs (injector/producer) is not applicable in tight reservoirs because of the low permeability of rock matrix and preferential flow of gas through fractures, bypassing the matrix oil (Carpenter 2018; Thakur 2019). Instead, the gas HnP process has been found as an effective technique to improve oil recovery in such reservoirs (Chen et al. 2014; Cronin et al. 2019). Field trials of natural-gas HnP have been implemented with promising results in the Eagle Ford Shale since 2013 (Aguilera and Vargas 2016; Rassenfoss 2017; Orozco et al. 2020). However, field pilots using enriched natural gas in Bakken Shale ended up with marginal improvements because of issues related to reservoir containment and complex geology (Kurtoglu 2013; Rassenfoss 2017).

Understanding oil-recovery mechanisms is crucial to optimize gas HnP processes implemented after the primary production of tight reservoirs. The recovery mechanisms involved in a gas HnP process include gas expansion, oil-viscosity reduction, oil swelling, and vaporization of oil components to the gas phase (Zick 1986; Alharthy et al. 2018; Carlsen et al. 2019). The transport of gas into the rock matrix is essentially controlled by gradients in pressure and chemical potential. Moreover, there may be enough time for gas diffusion if the injection phase takes 20 to 90 days as typically occurred in HnP field pilots (Carlsen et al. 2019; Jacobs 2019). There is still debate whether the mass transport of gas during the soaking period in an HnP process is dominated by advection or diffusion. N_{Pe} is a ratio of convective to diffusive forces. When $N_{Pe} < 1$, the mass transport is dominated by diffusion (Perkins and Johnston 1963; Hobbs and Ord 2015). Carlsen et al. (2019) and Cronin et al. (2019) suggested that the key mechanisms behind multiple-contact miscibility development in conventional gas-injection processes (e.g., vaporizing and/or condensing drive) are based on the advection-dominated transport within the matrix. In addition, they presumed that transport of gas into the matrix during the soaking period of the HnP process

*Corresponding author; email: dehghanpour@ualberta.ca

Copyright © 2020 Society of Petroleum Engineers

This paper (SPE 200341) was accepted for presentation at the SPE Improved Oil Recovery Conference, Virtual, 31 August–4 September 2020, and revised for publication. Original manuscript received for review 25 June 2020. Revised manuscript received for review 19 August 2020. Paper peer approved 1 September 2020.

in tight reservoirs may be a completely diffusion-dominated ($N_{Pe} \approx 0$) process, and thus, only first-contact miscibility is relevant. Other researchers conducted simulation studies on recovery mechanisms in shale and tight reservoirs and reported that diffusion mechanism dominates transport of gas into the Barnett shale matrix with permeability values of less than 10 nd (Olorede et al. 2017), and into the Bakken rock matrix with permeability in the range of 1 to 100 μd (Yu et al. 2015; Lashgari et al. 2019).

Several experimental studies have been conducted to evaluate oil recovery from tight rock samples (permeability in the range of μd) by gas HnP process using CO_2 (Habibi et al. 2017; Song and Yang 2017; Yu et al. 2017; Yassin 2019) and natural gas (Fu et al. 2019; Lou et al. 2019). However, there are very limited laboratory works to experimentally and visually investigate the role of gas diffusion and quantify dominant oil-recovery mechanisms involved in the natural-gas HnP process on ultratight rocks.

In this study, we performed laboratory tests and a N_{Pe} analysis to understand possible mechanisms that can be responsible for gas transport into and oil production from ultratight plugs during a gas HnP cycle. We used an ultratight plug from the Montney tight-oil formation and natural-gas samples (C_1 and a mixture of C_1/C_2 with the molar ratio of 70:30) for the HnP tests. The tests allow us to evaluate mechanisms controlling gas transport into the oil-saturated plug (advection vs. diffusion) during gas injection and soaking phases and mechanisms controlling oil recovery from the plug during the whole process.

Hypotheses Related to Oil-Recovery Mechanisms in the Gas HnP Process. Fig. 1 shows the sequence of hypothesized events responsible for gas transport into and oil production from the matrix during a HnP cycle in a tight-oil reservoir.

1. At initial conditions, fractures and matrix are at thermodynamic equilibrium and saturated with oil and solution and/or free gas depending on pressure and temperature. Usually, gas HnP is implemented after primary production, and thus, most of the leaked-off fracturing water is expected to be cleaned up. Therefore, the effect of water on phase-behavior calculations is assumed to be minimal.
2. In the “huff” phase, gas is injected into the well and is mainly transported through high-permeability fractures. Because the injection phase may take 20 to 90 days, advective and diffusive transports are responsible for gas flow into the rock matrix. A dynamic process of gas/oil mixing occurs near the fracture/matrix interface, resulting in vaporization of oil components to the gas phase and oil swelling. The contribution of oil-viscosity reduction caused by gas dissolution is expected to be insignificant because tight-oil viscosity is usually low at reservoir conditions. The gas-injection process completes when a targeted gas volume or injection pressure is achieved.
3. In the early soaking period, advection and diffusion remain the main gas-transport mechanisms. As the soaking period progresses, gas may penetrate deeper into the matrix by the diffusive transport and swell the oil. Soaking times of 5 to 30 days are typically applied in field pilots (Jacobs 2019).
4. During the depressurization phase, gas expansion is expected to be the dominant recovery mechanism. The expansion of the leaked-off gas (the gas transported into the matrix during injection and soaking periods) with reducing the pressure in the fractures may lead to a comingled flow of oil and gas toward the fracture face. The production period may take 60 to 100 days in field practices (Jacobs 2019).

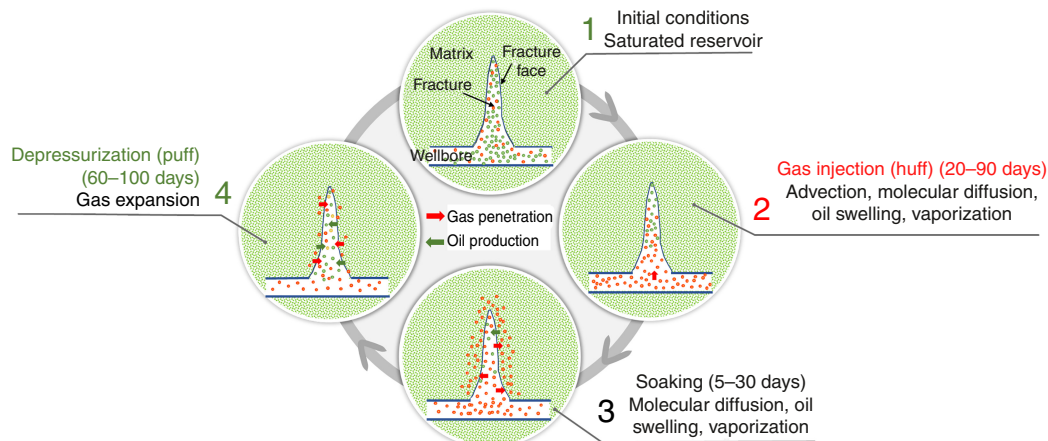


Fig. 1—Schematic of gas-transport and oil-recovery mechanisms during the gas HnP process.

Materials

Core Samples. The plug used in this study is from a well drilled in the Montney tight-oil formation in northwestern Alberta with the petrophysical properties listed in Table 1. Because the objective of the study is to compare the effects of gas composition and the differential pressure between injected gas and the plug ($\Delta P_i = P_g - P_o$) on gas-transport and oil-recovery mechanisms, the plug is reused to eliminate effects of heterogeneity.

Measured Depth (m)	Air Permeability, k_{air} (nd)	Porosity, Helium (% Bulk Volume)	Grain Density (kg/m^3)	Diameter (cm)	Length (cm)
2452.33	60	3.5	2.73	3.6	6.3

Table 1—Petrophysical properties of the plug.

After the coring operation, the whole core was cut into 1-m cylinders. Cylindrical plugs were then cut horizontally from the cylinders. The plug used in this study and the offset samples used for petrophysical characterization were cut from the same cylinder and at the same depth. The offset samples were cleaned using a Dean-Stark solvent extraction system before performing routine core analysis. Their porosity and air permeability were measured by helium porosimetry and pulse-decay techniques, respectively.

Broken pieces collected during cutting the plugs were used for X-ray diffraction analysis, assuming that their mineralogy is similar to that of the plug. **Table 2** lists the mineralogy of the plug obtained from X-ray diffraction analysis. Quartz (44 wt%) is the dominant mineral, followed by dolomite (14%), plagioclase feldspar (9%), potassium (K) feldspar (10%), and pyrite (5%). Clay minerals (illite/smectite and illite/mica mixed layers) account for 18 wt% of the whole rock weight.

Mineral	wt%
Quartz	44
K-feldspar	10
Plagioclase feldspar	9
Dolomite	14
Pyrite	5
Total clay	18
Total	100
Clay minerals	Relative clay (%)
Illite-smectite	66
Illite-mica	34
Total	100

Table 2—Mineralogy of the plug from the X-ray diffraction analysis.

Fig. 2 shows mercury-injection capillary pressure data of the plug. The median pore-throat size is 0.016 μm . The pores are classified as mainly mesopores (76% of the total pore space) according to the pore-size classification of the International Union of Pure and Applied Chemistry (Sing et al. 1985). It is well-known that part of the pores (small micropores) cannot be detected by the mercury-injection capillary pressure technique because of pore-accessibility issues.

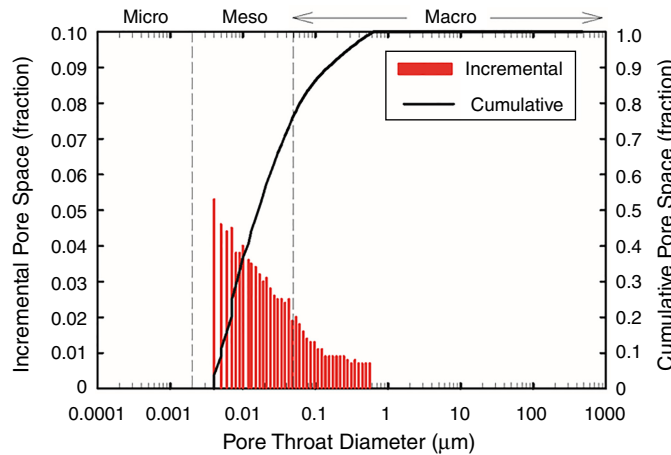


Fig. 2—Pore-throat size distribution from the mercury-injection capillary pressure data.

Fluid Samples. We used a dead oil sample from a production well located in the same zone as the cored well in the Montney Formation. The HnP experiments were conducted at $P_{\text{set}} = 137.9$ bar and $T_{\text{set}} = 50^\circ\text{C}$. The density and viscosity of the oil sample at atmospheric pressure (P_{atm}) and T_{set} are 818.5 kg/m³ and 2.82 mPa·s, respectively. C₁ and C₂ samples used in this study have a purity of 99.99%. The molecular weight of the oil is measured to be 209 g/mol. Further information on fluid characterizations, that is, compositional analysis, constant-composition-expansion data, and measured gas/oil minimum miscibility pressure (MMP), are presented elsewhere (Tran et al. 2020).

Method

Experimental Setup. We performed HnP tests on an oil-saturated plug at P_{set} and T_{set} to investigate mechanisms that control gas transport into and oil production from the plug at different phases of the HnP process. **Fig. 3** illustrates schematically the natural-gas HnP process conducted on an oil-saturated plug. The plug was coated by silicone to allow only one end-face open for gas and oil transports, mimicking the fracture face shown in Fig. 1. Moreover, the coating is expected to reduce the ratio of surface area in contact with gas to the gas volume. Here, we calculated oil RFs for comparing and ranking different recovery mechanisms. To evaluate the effects of gas composition on gas-transport and oil-recovery mechanisms, C₁ and a mixture of C₁ and C₂ with the molar ratio of 70:30 were used as injected gases. Bulk-phase experiments to characterize the interactions of these two gas samples with this Montney oil are presented elsewhere (Tran et al. 2020).

Table 3 lists the experimental conditions of two sets of tests (Sets 1 and 2). The pressure values in Table 3 and subsequent sections are gauge pressure. The main difference between Sets 1 and 2 is the value of ΔP_i , which is defined as the difference between injected-gas pressure ($P_g = P_{\text{set}}$) and initial pressure of the oil in the plug (pore pressure or $P_o = P_i$). For Set 1 with $\Delta P_i \approx 138$ bar, gas transport

is controlled by both advection and diffusion, representing injecting gas at pressures above the current reservoir pressure. For Set 2 with $\Delta P_i \approx 4$ bar, the advective flow is significantly smaller, representing injecting gas at the current reservoir pressure. The selected P_{set} values are below MMP of the gas/oil systems (301.03 bar for oil/C₁ and 188.99 bar for oil/C₁/C₂ with 30-mol% C₂).

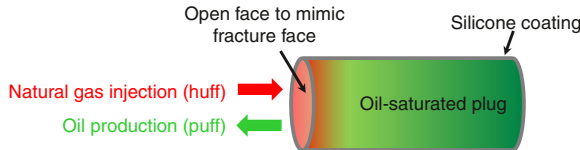


Fig. 3—Schematic of fluid flow through the open face of the oil-saturated plug during the natural-gas HnP process.

Set	Injected Gas	P_i (bar)	P_{set} (bar)	$\Delta P_i = P_{\text{set}} - P_i$ (bar)
1	C ₁	0	138.58	138.58
	C ₁ /C ₂ :70:30	0	138.52	138.52
2	C ₁	134.45	138.44	3.99
	C ₁ /C ₂ :70:30	134.43	138.37	3.94

Table 3—Initial conditions of the HnP tests. The temperature is kept at 50°C during the tests.

The tests were conducted using a high-pressure, high-temperature visualization cell schematically illustrated in **Fig. 4**. As illustrated in Fig. 3, only one end of the plug is open for contact with gas during injection, soaking, and depressurization periods. The internal volume of the cell was reduced from 587 to 390 cm³ (by placing solid blocks) to reduce the volume ratio of injected gas to oil in the plug, and to stabilize the plug during the gas injection. The clearance between the open face and sight glass was kept approximately at 1 to 2 mm. The small clearance was designed to avoid effects of light refraction during image capturing and video recording. More details about the specifications of the visualization cell can be found elsewhere (Yassin et al. 2018).

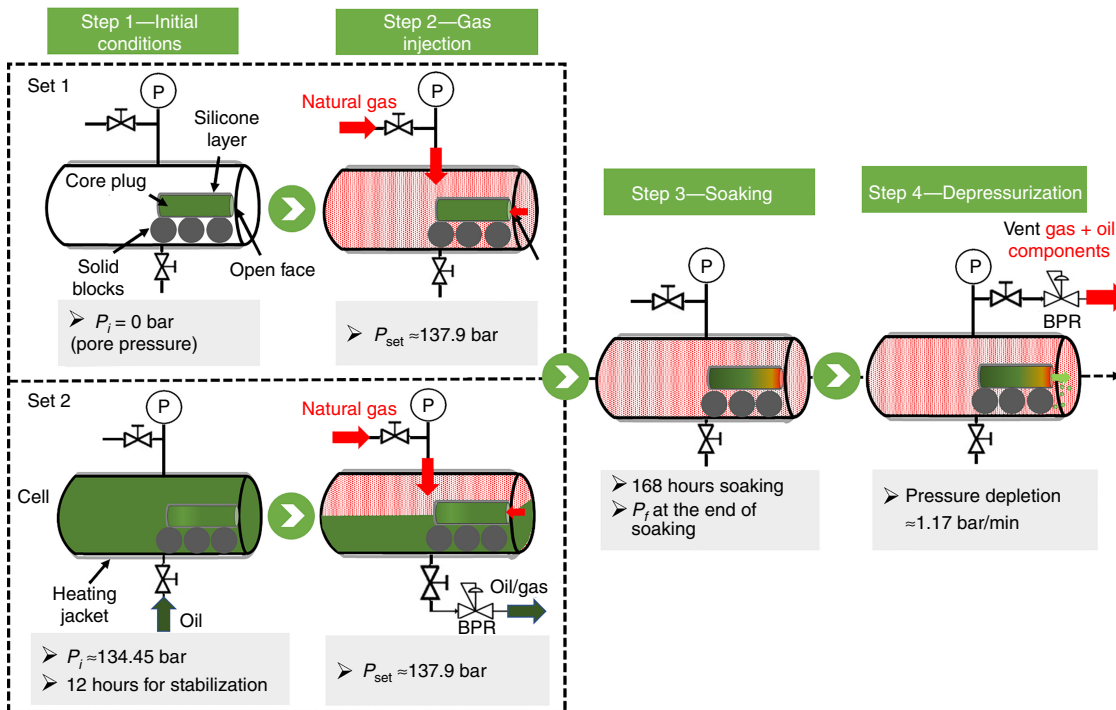


Fig. 4—Experimental setup and procedure for conducting HnP tests at T_{set} . P and BPR stand for pressure and backpressure regulator, respectively. Initial pore pressure, P_i , in Set 1 is atmospheric pressure, while it is ≈ 134.45 bar in Set 2.

The plug used in this study has a high volume of mesopores (76% of the total pore space) and a relatively high content of clays (18 wt%). Therefore, gas adsorption might occur and influence the gas transport during the HnP experiments. In an experiment to measure the adsorption of C₁ on montmorillonite, kaolinite, and illite clays, Liu et al. (2013) reported that C₁ was adsorbed only on the external surface of kaolinite and illite; however, adsorption occurred in both external surface and interlayer space of montmorillonite. It is important to mention that the plug was reconditioned (i.e., dried under vacuum pressure at 90°C in the cell for 2 days), resaturated with the reservoir oil, and weighed before starting a new test. The reconditioning might help release most of the residual oil [oil components trapped inside nanopores after pressure-depletion phase (Bui and Akkutlu 2017)] and gas in the plug before starting the next HnP experiment.

Experimental Procedure. The experimental procedure for the natural-gas HnP process includes four steps: (1) setting up initial conditions, (2) gas injection (huff), (3) soaking, and (4) depressurization (puff) process as demonstrated in Fig. 4.

Step 1, saturating and aging the plugs to restore reservoir conditions, includes the following substeps:

1. The plug was not cleaned by any solvents to remove residual oil and connate water. The use of high boiling point solvents; for example, toluene in the Soxhlet extraction, may cause significant dehydration of clay-bound water, dissolving of organic materials, and an increase in helium porosity resulting from possible opening of isolated micropores (McPhee et al. 2015). Instead, the plug was dried in an oven at 90°C until a stable weight was recorded over time. It is worth noting that some residual hydrocarbons and also salts might remain in the plug after the drying process.
2. The oil sample was filtered using a 1-μm filter paper to remove solid impurities.
3. The plug was vacuumed and aged in the oil at $P = 206.84$ bar and $T = 50^\circ\text{C}$ for 2 days. The ratio of imbibed oil volume by forced imbibition to the pore volume calculated by helium porosity is approximately 1.24 for the plug (2.79 vs. 2.24 cm³). The observed difference between pore volume (PV) values may be caused primarily by sample heterogeneity. The imbibed oil volume of 2.79 cm³ was used as the PV and initial oil volume in the oil-recovery calculations.
4. Except for the open face, other sides of the plug were coated by a layer of silicone with a thickness of approximately 0.6 mm. Afterward, the plug was weighed again and used for the tests.
5. The silicone coating was repeated after each test to ensure the integrity of the coating layer. The tested gas might permeate through the coating layer due to pressure difference, affecting mass transport during the experiments. Sadrzadeh et al. (2011) reported that an increase of 5.07 bar in the pressure difference on silicone membranes increases the permeability of gases (C₃H₈, CH₄, and H₂) through the membranes.
6. The temperature of the cell and accumulators were set at T_{set} by using heating jackets.
7. The tests were conducted under two different initial pore-pressure conditions to examine effects of advective and diffusive gas transports into the plug:
 - Set 1: The oil-saturated plug was transferred from the aging accumulator to the heated visualization cell. The cell was then vacuumed and ready for the gas injection phase.
 - Set 2: The cell was filled with oil and pressurized up to $P_i \approx 134.4$ bar. The system was left static for 12 hours to allow for pressure and temperature stabilization.

Step 2, gas injection (huff) process, includes the following substeps:

1. Set 1: After completing the vacuum step, the gas sample was immediately introduced into the cell from the top valve to reach P_{set} and minimize oil production from the plug caused by vacuum conditions. The oil production occurs because the pressure inside the plug was expected to be higher than the cell's pressure.
2. Set 2: A backpressure regulator (BPR) was installed at the bottom of the cell to control the discharge pressure. The BPR was set at P_i before starting the test. The gas sample was injected into the cell from the top valve at a pressure higher than the BPR's set pressure (by ≈ 4 bar) to gradually displace the oil. The gas injection ended when no more oil was observed from the outlet. All valves were then closed to start the soaking period.

Step 3, soaking process, includes soaking the plug in the gas samples for 168 hours (≈ 7 days). This soaking period was deemed sufficient to investigate the mechanisms responsible for gas transport into the plug, and the possibility of oil production by total-system compressibility, vaporization, oil-swelling, and gas-expansion mechanisms. In field practices, Jacobs (2019) reported that a soaking time of 5 to 20 days in a gas HnP process yields the highest oil recovery.

Step 4, depressurization (puff) process, includes venting the gas through the top valve and reducing the cell's pressure (at an average depletion rate of ≈ 1.17 bar/min) from the final soaking pressure P_f to P_{atm} using the BPR. According to Mouli (1989), the average depletion rate of experiments reported in the literature is often much greater than that in the field. The author also reported that an increasing depletion rate lead to a faster increase in critical gas saturation S_{gc} and higher oil recovery.

To determine the composition of the vented gas, it was collected using three gas cylinders (total volume of 1100 cm³) with pressures of 68.95, 35.85, and 15.16 bar for gas chromatography (GC) analysis. A predetermined amount of gas from each cylinder was collected and injected into a gas analysis bag for compositional analysis. The resulting composition and concentration (in cm³/m³ unit) of each oil component were reported. The concentration of the oil components had an accuracy of ± 0.1 cm³/m³. The total volume of vaporized oil of each test was obtained by multiplying the total oil-component concentration by the total volume of the three cylinders.

Images and videos of the open face were captured during gas-injection, soaking, and depressurization phases. The final oil RF was calculated by the weight-balance method. The reading accuracy of the balance is 0.1 mg. It is worth noting that the volume ratio between the gas in the cell and the oil in the plug at P_{set} is significantly high (390 vs. 2.79 cm³), leading to an overestimation of oil RF compared with field cases.

Results and Discussions

Here we present the results of soaking the oil-saturated plug in C₁ and a mixture of C₁/C₂ (70:30 mol%) for ≈ 168 hours at T_{set} . **Table 4** lists results of the four HnP tests. The P_i of the plug before starting gas injection in Sets 1 and 2 are approximately 0 and 134 bar, respectively. The leaked-off gas is calculated based on the difference in molar mass of gas in the cell at initial conditions P_{set} and at the end of the soaking process P_f . We assume that partial pressures created by vaporized oil components at P_f are negligible. For the same gas composition, the leaked-off gas for the tests with $\Delta P_i > 0$ bar is higher than that with $\Delta P_i \approx 0$ bar. For instance, the leaked-off gas increases by approximately 45% (0.045 vs. 0.031 mol) and 8% (0.104 vs. 0.096 mol) in C₁ and C₁/C₂ tests, respectively. Adding 30 mol% of C₂ to the injected gas increases the leaked-off gas by 131% (0.104 vs. 0.045 mol) in Set 1 and 210% (0.096 vs. 0.031 mol) in Set 2.

Quantifying Gas-Transport Mechanisms during Injection and Soaking Phases. During the soaking period, pressure in the cell declines resulting from gas transport into the oil-saturated plug. **Fig. 5a** shows pressure-decline profiles during the soaking period of the four HnP tests. The time span of the soaking period is approximately 168 hours. For the same gas composition, the absolute pressure-drop (from P_{set} to P_f) values in Set 1 are higher than those in Set 2. For instance, they are 5.28 and 4.75 bar in Set 1-C₁/C₂ test and Set 2-C₁/C₂ test, respectively. The observed difference is attributed to the stronger advective gas transport into the plug in Set 1.

We compare pressure-decline profiles of the HnP tests with those of bulk-phase tests in **Fig. 5b** (Tran et al. 2020) to investigate the hindrance of gas dissolution into oil by rock matrix. Equilibrium pressures, P_{eq} , of the bulk-phase oil/C₁ and oil/C₁/C₂ tests are 114.07 and 106.95 bar, respectively. The time to reach P_{eq} and pressure-drop value in the oil/C₁/C₂ test are shorter and higher than those in the oil/C₁ test (67 vs. 60 hours and 31.09 vs. 23.53 bar), respectively. Absolute pressure-drop values of HnP tests are approximately one order of magnitude lower than the bulk-phase ones, for example, 2.55 vs. 23.53 bar in Set 1-C₁ and oil/C₁ tests.

Set	P_{set} (bar)	Injected Gas	Initial Conditions		End of Soaking Period			End of Test Produced Oil (mol)
			Initial Oil (mol)	Injected Gas (mol)	P_f (bar)	Bulk Gas (mol)	Leaked-Off Gas (mol)	
1	138.58	C_1	0.011	2.293	136.03	2.248	0.045	0.004
	138.52	$C_1/C_2:70:30$	0.011	2.623	133.34	2.519	0.104	0.005
2	138.44	C_1	0.011	2.291	136.65	2.260	0.031	0.003
	138.37	$C_1/C_2:70:30$	0.011	2.620	133.62	2.524	0.096	0.004

Table 4—Results of the four HnP tests.

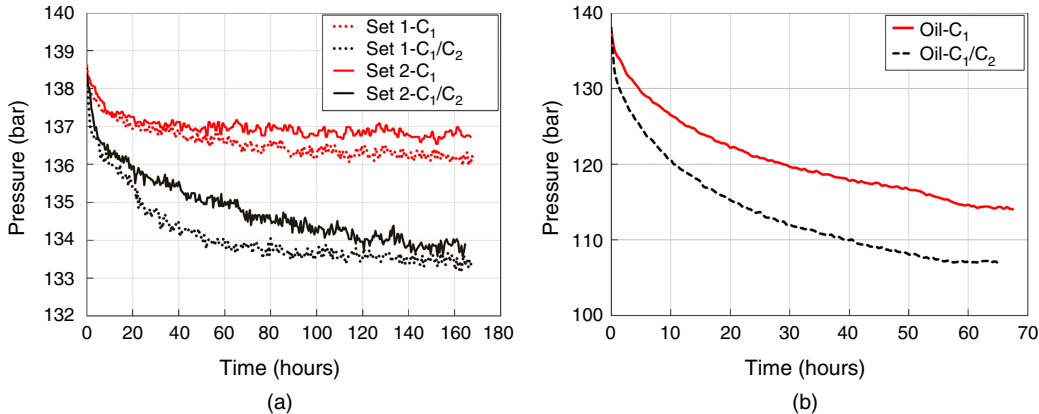


Fig. 5—Pressure-decline profiles during (a) ≈ 168 hours soaking period of HnP tests, and (b) soaking period of oil/C₁ and oil/C₁/C₂ tests at T_{set} (Tran et al. 2020).

The similarity of pressure-decline profiles between the HnP and bulk-phase tests suggests that they may experience similar gas-transport mechanisms. The bulk-phase pressure-decline trend is similar to the HnP tests with a sharp decrease at the beginning and a gradual decline toward the end of the soaking period. At the early soaking period in bulk-phase tests, pressure decline is affected by the resistance to mass transfer at the gas/oil interface (Rasmussen and Civan 2009; Pacheco-Roman and Hejazi 2015). Moreover, there is a higher concentration gradient of gas near the gas/oil interface, resulting in faster gas transport and high pressure drop in the early soaking period. When the soaking progresses, molecular diffusion dominates gas transport into the oil. A similar gas-transport process is believed to occur during the soaking period of HnP tests. The pressure drop in Set 1 is higher than that in Set 2 because of the effect of stronger advective flow in a region close to the plug's surface. During the HnP process in tight reservoirs, pressure-driven advective gas transport is dominant during gas-injection and early soaking periods (Alharthy et al. 2018), while molecular diffusion is dominant when the soaking period progresses (Hoteit and Firoozabadi 2009; Javadpour 2009; Yu et al. 2015). In a modeling study of production from shale reservoirs, Ozkan et al. (2010) reported that Darcy-dominated flow occurs in the region close to the fracture/matrix interface, and the diffusive flow dominates in the matrix with permeabilities in nanodarcy range.

In both HnP and bulk-phase tests, adding C₂ significantly increases the pressure-decline rate. In Fig. 5b, the lower P_{eq} in oil/C₁/C₂ compared to that in the oil/C₁ test is attributed to the higher solubility of C₂ in oil compared to C₁. At the equilibrium, the time to reach P_{eq} in the oil/C₁/C₂ system is shorter than that in the oil/C₁ system, suggesting a higher diffusion rate of C₂ in the oil. According to Li et al. (2020), the solubility and diffusion coefficient of C₂ in Bakken oil (under 90 bar and 109.8°C) are approximately 8.5 times (≈ 9 vs. ≈ 77 g/100 g) and 2.7 times ($\approx 3 \times 10^{-9}$ vs. 8.2×10^{-9} m²/s) higher than those of C₁. This observation is complemented by bulk-phase visualization tests (Fig. A-1 in Appendix A). In the oil/C₁ test, vaporizing flows (upward red arrows) of oil components to the gas phase occur during the gas-injection phase (Fig. A-1a), while vaporizing and condensing flows coexist during the same period in the oil/C₁/C₂ test (Fig. A-1b). The appearance of the condensing flows (downward green arrows) of C₁, C₂, and vaporized oil components into the oil phase means stronger gas transport into the oil phase. In addition, the vaporizing flows become stronger by adding 30-mol% C₂ to the injected gas. Videos captured during the gas-injection phase of the bulk-phase tests are provided in the Supplementary Material in Appendix B.

Quantification of Mass-Transport Mechanisms during Soaking Period. To evaluate contributions of advection and diffusion during the soaking period, we model and calculate N_{Pe} of the four HnP tests, as described in Appendix C. The estimated bulk-phase diffusion coefficients D using Eq. C-3 are 5×10^{-9} m²/s and 6.5×10^{-9} m²/s for oil/C₁ and oil/C₁/C₂ tests, respectively. The results are in agreement with published literature (Fu et al. 2019; Lou et al. 2019; Li et al. 2020). We divided the pressure-decline periods of HnP tests to early-time and late-time periods by the k -plane clustering method (Bradley and Mangasarian 2000) and piecewise linear regression as shown in Appendix C (Fig. C-1). Table 5 lists the calculated values of average pressure drop, Darcy velocity, and N_{Pe} for the four HnP tests at early and late times. At the early times, N_{Pe} ranges from 1.82 to 3.03, suggesting that both advective and diffusive transports coexist in the system. Nevertheless, N_{Pe} of Set 1 is 12 to 15% higher (stronger advection) than Set 2. At the late times, N_{Pe} ranges from 0.26 to 0.62, indicating the dominance of molecular diffusion. Changes in the N_{Pe} vs. time for different HnP tests is shown in Appendix C (Fig. C-2). Although the tests in Set 2 are designed with minimal ΔP_i , pressure changes during the gas/oil displacement (in the injection phase) could be the cause of higher-than-expected advection in the early times.

Visualization and Quantification of Oil-Recovery Mechanisms during Gas-Injection and Soaking Phases. Fig. 6 shows the surface of the oil-saturated plug (denoted by surface) corresponding to the four stages of the four HnP tests. Videos captured during the gas-injection and depressurization phases of the HnP tests are provided in the Supplementary Material in Appendix B.

- Step 1. Images show the surface at initial conditions of Sets 1 and Set 2 (at P_i , T_{set}). They are all wet by the oil phase. The surface in Set 2 is unclear because the plug was fully immersed in the oil at P_{set} .
- Step 2. Images show the surface at the end of the gas-injection phase (138.58 and 138.52 bar in Set 1-C₁ and -C_{1/C₂}, 138.44, and 138.37 bar in Set 2-C₁ and -C_{1/C₂} tests, respectively). The total time required for the gas-injection process is approximately 0.3 hours in Set 1 and 0.22 hours in Set 2. The surface changes from wet to partially dry in Set 1, while it remains wet by the oil phase throughout the gas-injection phase in Set 2. Because the clearance between the surface and the sight glass is fairly small, the wet areas highlighted by the yellow circle in Set 2-C₁ may be caused by residual oil resulting from nonuniform gas/oil displacement during the injection phase. This residual oil mainly exists at the interface of the coating layer and surface, caused by the weak bonding between the plug and coating layer, leading to an edge effect.
- Step 3. Images demonstrate the surface after approximately 168 hours of soaking in C₁ and a mixture of C_{1/C₂}. During the soaking period, the surface becomes completely dry in Set 1, while it is partially dry in Set 2.
- Step 4. Images show comingled flows of gas and oil on the surface during the depressurization process. The observed nonuniform oil production in Set 2 may be caused by the edge effect.

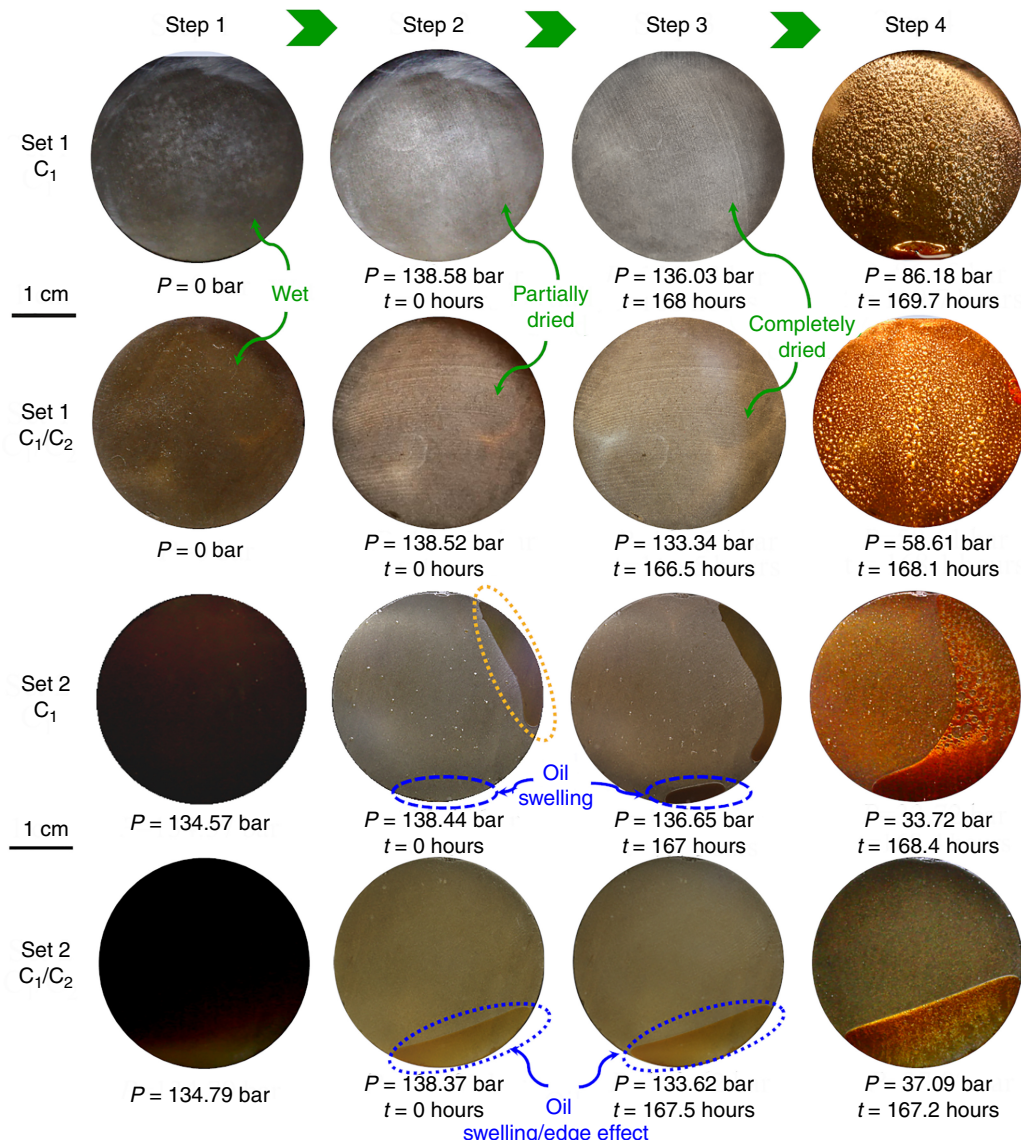


Fig. 6—Images of the plug surface during initial conditions (Step 1), gas injection (Step 2), soaking (Step 3), and depressurization (Step 4) of all the tests at T_{set} .

The experimental results show that the HnP process involves four recovery mechanisms, including total system compressibility, vaporization of oil components, oil swelling, and gas expansion.

Total System Compressibility. This recovery mechanism is caused by the presence of ΔP , and is only expected to occur in Set 1. The wet surface during gas injection (from Steps 1 to 2 in Fig. 6 shown by the video images provided in Appendix B, Supplementary Material) is caused by compressibility when pressurizing the plug from P_i to P_{set} . The oil production during the injection phase of Set 1 is attributed mainly to the change in initial pore and oil volume caused by total system compressibility. Because the plug is very tight and the gas-injection duration is short, most of the oil inside the pores farther from the surface is still at approximate to P_i . Therefore, we can assume that oil recovery by oil compressibility is negligible. Other recovery mechanisms, such as vaporization and oil swelling, may also occur in the injection phase and will be discussed in the next subsections. We calculate the change of PV caused by rock compressibility at T_{set} by

where $V = 2.79 \text{ cm}^3$ is the initial PV, ∂V is the change in PV (cm^3), c_f is the isothermal coefficient of rock compressibility (1/bar), and $\partial P \approx 137.9 \text{ bar}$ is the change in pressure when pressurizing the cell from P_i to P_{set} . c_f at the porosity of 3.5% is $1.48 \times 10^{-4} \text{ 1/bar}$ (Geoscience BC 2011). The estimated ∂V using Eq. 1 is 0.06 cm^3 . Lan et al. (2017) and Davudov and Moghanloo (2018) reported that PV compressibility of gas-shale samples changes as a function of effective stress and its change affects pore connectivity, permeability, and gas recovery.

Parameter Description	Value				
	Set 1-C ₁	Set 1-C ₁ /C ₂	Set 2-C ₁	Set 2-C ₁ /C ₂	
Porosity, ϕ (-)	3.5×10^{-2}	-	-	-	
Permeability, k (m ²)	5.92×10^{-20}	-	-	-	
Oil viscosity, μ (Pa·s)	9×10^{-3}	-	-	-	
Core-plug length, L (m)	6.3×10^{-2}	-	-	-	
Effective diffusion coefficient, D_{eff} (m ² /s)	1.75×10^{-10}	2.28×10^{-10}	1.75×10^{-10}	2.28×10^{-10}	
Pécelt Number Calculations					
Early times	Pressure drop, $\frac{\partial p}{\partial t}$ (Pa/s)	-3.89	-18.20	-2.93	-14.45
	Darcy velocity, u (m/s)	5.05×10^{-9}	1.09×10^{-8}	4.39×10^{-9}	9.75×10^{-9}
Late times	Péclet number, N_{Pe} (-)	1.82	3.03	1.58	2.70
	Pressure drop, $\frac{\partial p}{\partial t}$ (Pa/s)	-0.14	-0.76	-0.08	-0.30
	Darcy velocity, u (m/s)	9.46×10^{-10}	2.24×10^{-9}	7.25×10^{-10}	1.40×10^{-9}
Péclet number, N_{Pe} (-)					
		0.34	0.62	0.26	0.39

Table 5— N_{Pe} calculations for 1D transport of natural gas into the oil-saturated plug. The values of porosity, permeability, oil viscosity, and core-plug length are the same for all the HnP tests.

Vaporization of Oil Components. Fig. 7 compares the mole fraction of oil components (C_5 to C_{12}) vaporized into the gas phase during the HnP experiments, obtained by GC analysis of the collected gas samples. Because the mole fraction of gas in the collected samples is significantly high compared to the vaporized oil components, only mole fractions of vaporized oil components are normalized and plotted for comparison. In particular, C_8 to C_{10} components account for more than 70 mol% of the vaporized oil volume. The volumes of vaporized oil in Set 1- C_1 , Set 1- C_1/C_2 , Set 2- C_1 , and Set 2- C_1/C_2 are 0.02, 0.05, 0.01, and 0.03 cm^3 , respectively. The molar ratio of the vaporized oil to the original oil in the plug is 0.47 to 1.68 mol%.

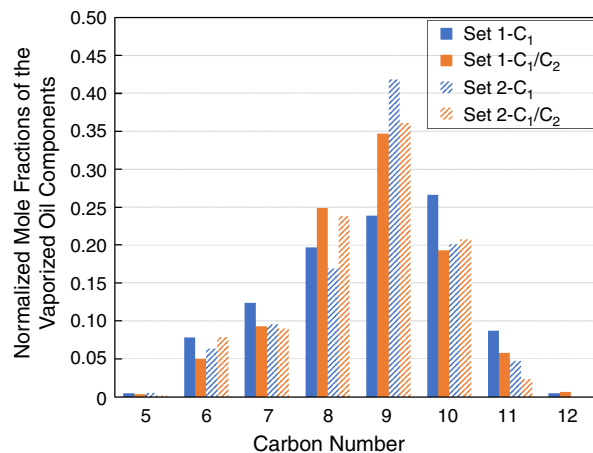


Fig. 7—Normalized mole fractions of the vaporized oil components from the GC analysis.

The vaporization is qualitatively and quantitatively evaluated using visualization data in Fig. 6 and GC analysis of produced gas samples. The change of the surface state from wet to partially/completely dry during injection and soaking periods suggests vaporization of oil components from the surface to bulk-gas phase. In Fig. 7, the amount of vaporized oil in the C_1/C_2 tests are higher than that in the C_1 tests. This can be explained by the higher solubility of C_2 in oil compared to C_1 . Moreover, the developed miscibility conditions through vaporizing- and/or condensing-gas drive may contribute to incremental oil production by vaporization in Set 1. In Set 2, the vaporization during injection and soaking periods is expected to be marginal, because of the weaker advective gas transport. In such, the amount of vaporized oil in Set 2 may be caused by the mixing of gas and bulk oil outside the plug during the displacement process.

Oil Swelling. Signs of oil swelling are observed during the injection and soaking periods in Sets 1 and 2. As mentioned in the Total System Compressibility section, the wet surface during gas injection in Set 1 may be partially caused by oil swelling. However, the

surface remains dry during the soaking period. This suggests that oil recovery by the swelling mechanism may be insignificant. In Set 2, signs of oil swelling appear during the injection and soaking phases. They are highlighted by the blue circles on the images for Steps 2 and 3. However, the wet area at the bottom part of the surface in Set 2-C₁/C₂ may be influenced by the edge effect. The observed oil swelling during the injection and soaking phases is in agreement with the results of gas HnP experiments performed on Bakken rocks by Hawthorne et al. (2013). The authors reported that oil swelling was higher during the soaking period compared to that during the gas-injection phase.

The results of bulk-phase tests to visualize interactions at the gas/oil interface show potential of oil swelling caused by gas dissolution into the oil. The volume of the oil in oil/C₁ and oil/C₁/C₂ bulk-phase tests expand 8 and 28% after 67 and 60 hours soaking, respectively. The higher oil swelling by the mixture of C₁ and C₂ is attributed to the higher solubility of the gas mixture in oil compared to C₁ solubility in oil. Details of experimental conditions and results can be found in Appendix A (Fig. A-2). The contrast in the extent of oil swelling in bulk-phase and HnP tests suggests that there is a considerable hindrance to gas transport by the rock matrix.

Gas Expansion. This production mechanism is controlled by the expansion of leaked-off gas during depressurization phase. Comparing oil production on the surfaces at different phases of the HnP process suggests that gas expansion is the dominant recovery mechanism. However, it is difficult to quantify oil-production volume by the gas-expansion mechanism using this experimental setup. The recovery performance under this important mechanism will be discussed in a later section.

Final Oil Recovery. Fig. 8 compares oil RFs measured by the weight-balance method for Sets 1 and 2. For the same gas composition, oil recovery in Set 1 is higher than that in Set 2. For example, RF of Set 1-C₁ is higher than that of Set 2-C₁ by 21.9% (35.86% vs. 29.41%). For the same ΔP_i conditions, adding 30-mol% C₂ to the gas mixture increases oil recovery by 14.44% (from 35.86 to 40.88%) in Set 1 and 21.93% (29.41 to 35.72%) in Set 2, respectively.

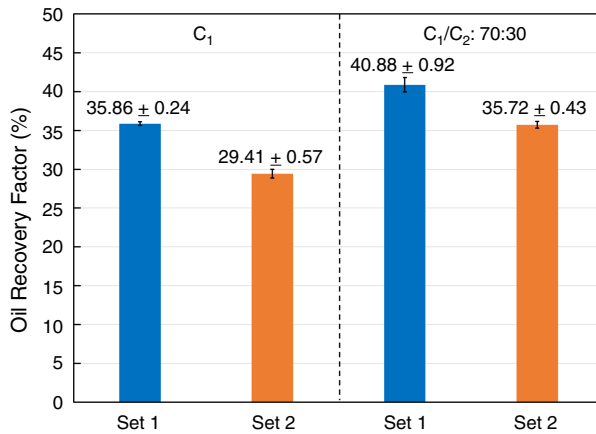


Fig. 8—Oil RFs from the HnP tests measured by the weight-balance method.

The mechanisms responsible for the oil recovery presented in Fig. 8 include the total system compressibility, vaporization, oil swelling, and gas expansion. Table 6 lists the oil-recovery volume and percentage of contribution of each mechanism in the total oil recovery. The oil RFs are calculated and compared based on the same initial oil volume in all sets:

- The oil production by total system compressibility is calculated by Eq. 1. Because ΔP_i in Set 2 is set to be zero, no oil production caused by compressibility is reported.
- The oil production by vaporization is obtained from GC analysis.
- Because it is difficult to quantify oil production by solely gas expansion or oil swelling, they are reported as a combined gas-expansion/oil-swelling mechanism. However, oil recovery by gas expansion is significantly higher than that by oil swelling. The amount of leaked-off gas is one of the important factors affecting the recovery by the gas-expansion mechanism. The oil produced by this mechanism is calculated by subtracting the oil volume produced by total system compressibility and vaporization from the total oil production.

Set	Injected Gas	Total System Compressibility		Vaporization		Combined Gas Expansion/Oil Swelling		Total Oil Production (cm ³)
		Volume (cm ³)	Total (%)	Volume (cm ³)	Total (%)	Volume (cm ³)	Total (%)	
1	C ₁	0.06	5.72	0.02	1.63	0.92	92.65	0.99
	C ₁ /C ₂ :70:30	0.06	4.99	0.05	4.03	1.04	90.98	1.14
2	C ₁	0	0	0.01	1.60	0.81	98.40	0.82
	C ₁ /C ₂ :70:30	0	0	0.03	3.00	0.97	97.00	1.00

Table 6—Oil production by different recovery mechanisms during the natural gas HnP experiments.

The highest percentage of oil production is by a combined gas-expansion/oil-swelling mechanism, followed by total system compressibility and vaporization. Combined gas expansion/oil swelling accounts for 90.98 to 98.4% of the total production, while vaporization is the least contributor with less than 4% of the total recovery in Sets 1 and 2. For the same gas composition, the total oil production in Set 2 is less than that in Set 1 because of the absence of oil recovery from total system compressibility and a weaker advective flow.

Oil-Recovery Mechanism during Depressurization Phase. The measured oil recovery (Table 6) and images of the surface showing significant oil production during the depressurization phase (Step 4 in Fig. 6) indicate that gas expansion is the dominant recovery mechanism in the natural-gas HnP process. The leaked-off gas expands and flows out of the plug, dragging oil along with it, under the induced pressure gradient during the depletion phase.

To determine states of the gas phase in the plug; that is, free and/or solution gas, at the end of the soaking period, we estimated saturation pressure P_{sat} and fractions of free and solution gas in the gas/oil systems using the Peng and Robinson (1978) equation of state (PR-EOS) that was calibrated against the constant-composition-expansion and MMP data (Tran et al. 2020). It should be noted that this quantification is to better understand the phase behavior of the gas/oil system before the depressurization and does not reflect the exact thermodynamic conditions in the plug. The density values of C_1 (under P_{set} , P_f , and T_{set}) are obtained from the National Institute of Standards and Technology (NIST 2018) chemical webbook. We used the flash calculation module in PVTsim software (Calsip A/S 2018) to calculate the gas density (under P_{set} , P_f , and T_{set}) and fractions of free and solution gas in the leaked-off gas. In addition, we used the saturation-point prediction module to predict P_{sat} of the gas/oil systems.

P_{sat} values and fractions of free/solution gas in the leaked-off gas are calculated using the calibrated PR-EOS based on three assumptions: because the gas volume in the cell is relatively high, the concentration of vaporized oil components is negligible; the changes in oil composition resulting from vaporization are insignificant; and the effects of nanoconfinement on phase behavior calculations are neglected. **Table 7** lists the estimated P_{sat} values and fractions of free/solution gas at the end of the soaking period for the four gas/oil systems. The molar ratio of gas/oil systems; that is, leaked-off gas/original oil, used in the PR-EOS calculations is taken from Table 4. The mol% of gas/oil at P_f is estimated by performing flash calculations for the mixtures of leaked-off gas/original oil at respective P_f and T_{set} . Based on the experimental conditions of the HnP tests (P_{set} and $P_f < P_{\text{sat}}$), the leaked-off gas exists in both solution- and free-gas states during the experiments. Two-phase equilibrium data from the flash calculations show a high fraction of free gas (0.61 to 0.74) in the pores at the end of the soaking period.

Set	Injected Gas	Mol% of Leaked-Off Gas/Original Oil	P_{sat} (bar)	Mol% of Gas/Oil at P_f	Leaked-Off Gas at the End of Soaking (fraction)	
					Free	Solution
1	C_1	80.25/19.75	281.29	58.97/41.03	0.73	0.27
	$C_1/C_2:70:30$	90.30/9.70	228.95	67.02/32.98	0.74	0.26
2	C_1	73.49/26.51	238.38	44.40/55.60	0.61	0.39
	$C_1/C_2:70:30$	89.62/10.38	226.83	64.73/35.27	0.72	0.28

Table 7— P_{sat} estimation by the calibrated PR-EOS and fractions of free/solution gas in the leaked-off gas at the end of the soaking period. The fraction of free gas is calculated by taking the ratio of mol% of gas at P_f and the mol% of leaked-off gas. For instance, it equals to $58.97/80.25 = 0.73$ in the Set 1-C₁ test.

Fig. 9a shows pressure-depletion profiles of the four HnP tests and images of gas/oil production during the depressurization phase in Set 1-C₁. It took approximately 2 hours (with an average pressure-depletion rate of 1.17 bar/min) to depressurize the gas/oil systems in Sets 1 and 2 from P_f to P_{atm} . Images of the surface in Set 1-C₁ test correspond to the onset of the depressurization, observing the early oil droplets on the surface, and significant production of gas and oil. The pressures at which the early oil droplets were observed in Sets 1 and 2 are approximately 124 and 117 bar, respectively. Fig. 9b shows the comingled flow of oil and gas driven by the gas-expansion mechanism in Set 2-C₁/C₂ test. The magnified image of the surface shows the evolution of gas bubbles at $t = 168.2$ hours and $P = 55.85$ bar. The gas bubbles evolve from the pores and flow upward (red arrows), dragging the oil upward before draining downward by gravity (blue arrow on the unmagnified surface). Gas bubbles coalesce and form bigger ones (yellow arrows) while moving upward.

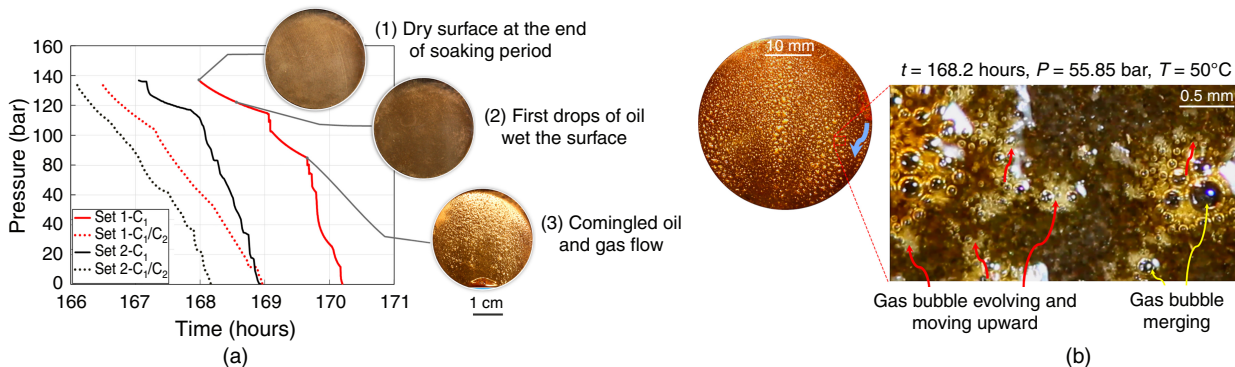


Fig. 9—(a) Pressure-depletion profiles and the images of gas/oil production on the surface during the depressurization phase in Set 1-C₁ test, and (b) the evolved gas bubbles, merged bubbles (yellow arrows), produced oil flowing upward (red arrows), and the produced oil draining downward by gravity (blue arrow) observed on the core surface during the depressurization phase of the Set 2-C₁/C₂ test.

During the depressurization phase, the solution gas evolves and merges with free gas, increasing the overall gas saturation. S_{gc} refers to the minimum gas saturation required for forming a continuous gas phase that can flow independently. When the pressure reduces to the point corresponding to S_{gc} , for example, 124.2 bar in Set 1-C₁ test, gas starts flowing toward the surface. One might notice a time delay of 0.46 hours for a pressure drop of 11.83 bar (from 136.03 to 124.2 bar) and for gas/oil production to be observed on the surface in Set 1-C₁ test (Fig. 9a). This production delay might be attributed to the process of solution gas evolution and coalescence of solution/free gas caused by reducing the cell's pressure. The observed oil production on the surface in Step 4 of Fig. 6 suggests that the

performance of oil recovery by gas expansion may depend on ΔP_i , the amount of leaked-off gas during injection and soaking periods, and the pressure-depletion rate. In a modeling study of produced-fluid composition redistribution during the depressurization phase in tight-oil reservoirs, Baek and Akkutlu (2019) reported that gas expansion is an important recovery mechanism and is pronounced in relatively large pores (>10 nm). Because the evolved gas is observed at several locations on the surface, the more the surface area in contact with the gas, the faster the oil can be recovered. Rassenfoss (2017) and Jacobs (2019) reviewed field-pilot data and suggested that the performance of gas HnP EOR in shales is controlled by the gas/rock contact area and the injection pressure.

Implications for the Gas HnP Field Practice. Start Time of the Gas HnP EOR. The results of this experimental study indicate that the application of the natural-gas HnP process on Montney ultralight rocks is technically feasible. The start time of the gas HnP EOR process is often a key question when planning a reservoir-development strategy. Injectivity is typically an issue if injection starts at the beginning of well life. It is because the formation pressure gradient is still high, resulting in less gas transported into the matrix. Injecting gas into a depleted reservoir would benefit from the total system compressibility and higher leaked-off gas and consequently oil recovery caused by the advective transport. Sanchez-Rivera et al. (2015) and Chen and Gu (2017) performed simulation studies of CO₂ HnP application in Bakken Shale. The authors reported that the potential of repressurization is not fully used if the operation starts early in the well life.

Shut-In Time. From the pressure-decline profiles in Fig. 5a, gas transport into the plug was pronounced for the first four days of the 7-day shut-in period. It means that a reasonable shut-in time to achieve high oil recovery might be less than 7 days. This observation is in agreement with the results of field pilots in which a shorter shut-in time (≈ 5 days) seems to yield better oil recovery than longer ones (Jacobs 2019).

Injection and Depressurization Strategy. The results of this laboratory study show that improved gas transport into the matrix and an appropriate depletion strategy are two key factors leading to high oil recovery. In the field application, the efficiency of the gas HnP process might be improved by increasing injection pressure and/or enriching the injected gas by intermediate hydrocarbon components. Increasing injection pressure would be recommended as the first and preferable choice. First, it is practical to inject at high-enough pressures to achieve miscible conditions. Second, a high injection pressure helps to spread out the gas farther from the matrix/fracture interface, thus increasing the surface area in contact with the gas. As mentioned in the Oil-Recovery Mechanism during Depressurization Phase section, the surface area created by fracturing operations significantly affects oil recovery by the gas-expansion mechanism. However, it may be difficult to achieve the MMP, for instance, 301.03 bar for oil/C₁, because this pressure may exceed the gas-compressor capacity and may lead to geomechanical complications, such as refracturing the formation. With the limitation of injection pressure, the enrichment of injected gas, for example by 30-mol% C₂ in this study, is a viable solution to increase oil recovery. In terms of the depletion strategy, choke-size control is needed to optimize the pressure-depletion rate. A too-fast pressure-depletion rate might lead to a rapid loss of energy from the gas expansion and bypassing the oil by high-velocity gaseous phase, while a too-slow one may end up with insufficient gas energy to drag the oil along its flowpaths.

Upscaling Experimental Data to Field Scale. The gas HnP experimental data need to be scaled up for predicting pilot-scale response. There are two popular methods for upscaling core-scale data. The first is by using dimensionless groups (e.g., dimensionless time) involving different transport mechanisms and reservoir properties (Li and Lake 1995; Wood et al. 2008; Li and Sheng 2017). Usually, a single type curve of oil recovery vs. a dimensionless group is generated for systems with different length scales. Another upscaling method involves scaling up mass-transport properties from a fine scale to a coarse scale (Leung and Srinivasan 2011; Hertel et al. 2018). Properties at the coarse scale are calculated by averaging those at the fine scale. Here reservoir heterogeneity is preserved, which is important for recovery performance. In both methods, the first step is to calibrate core-scale responses by performing numerical modeling. Then the calibrated model can be scaled up by one of the methods previously discussed. It should be noted that using more heterogeneous core samples in the experiments leads to more accurate scaled-up oil recovery.

Limitations

We present the following limitations:

- Silicone coating may not fully function under high-pressure and high-temperature conditions during the HnP experiments. Part of the coating layer may be soluble in oil at T_{set} in Set 2. This may cause nonuniform gas/oil displacement during the gas-injection and soaking phases, and oil production during the depressurization.
- The interactions of injected gas and the oil during the injection and soaking phases may strip out some intermediate and heavy components of the oil. The residual-oil components with higher molecular weight may not be completely removed by the drying process performed after each experiment.
- It is difficult to separately quantify oil recovery by the gas expansion and oil swelling by this experimental setup.
- Because of the nonuniform gas/oil displacement, there are still traces of oil left in the cell after the injection phase in Set 2. This amount of oil may vaporize and affect the GC analysis and the estimated oil recovery by the vaporization mechanism.
- The experimental database is limited because only one plug is used in this study. Therefore, future work is needed to solidify the findings related to gas-transport and oil-recovery mechanisms using plugs with a range of porosity and permeability. Additional works to evaluate oil recovery under different pressure-depletion rates and injection pressures; that is, above the MMP of the oil and gas mixture (C₁/C₂:70:30 mol%), are useful for field-pilot design.

Conclusions

We studied gas-transport and oil-recovery mechanisms during gas HnP processes in tight-oil reservoirs. We conducted gas HnP tests using an ultralight Montney core plug and natural-gas samples (C₁ and a mixture of C₁/C₂ with the molar ratio of 70:30) under reservoir conditions ($P = 137.9$ bar and $T = 50^\circ\text{C}$). In each test, we soaked the plug in the gas for approximately 168 hours using a visualization cell. We measured pressure decline during the soaking period, visualized oil production on the plug's surface, and calculated N_{Pe} to investigate mass-transport mechanisms (advection vs. diffusion) during injection and soaking phases and oil-recovery mechanisms during the whole process. The tests also allowed us to compare the effects of gas composition and initial differences between injected gas and pore pressures on gas-transport and oil-recovery mechanisms. Our key results are the following:

1. Advection-dominated transport was found to be the mechanism responsible for the transport of gas into the plug at early times of soaking period ($N_{Pe} = 1.58$ to 3.03). However, molecular diffusion is the dominant mechanism when the soaking progresses ($N_{Pe} = 0.26$ to 0.62). The advective-gas flow caused by differential pressure enhances mass transfer of gas into the plug during the injection and soaking periods, and consequently the oil recovery.

- From the four studied recovery mechanisms (total system compressibility, vaporization, oil swelling, and gas expansion), gas expansion is the dominant one, followed by total system compressibility, oil swelling, and vaporization.
- Expansion of free and solution gas during the depressurization period results in a significant comingled flow of gas and oil observed on the plug's surface. Therefore, the higher the amount of leaked-off gas during injection and soaking periods, the higher the oil recovery achieved by the gas-expansion mechanism.
- The enrichment of injected gas by C₂ (30 mol% in this study) leads to an increase of 131 to 210% in mass transport of gas into the plug as well as oil recovery.

Finally, the findings presented in this study provide a reasonable basis for operators to improve understanding of gas-transport and oil recovery mechanisms involved in the gas HnP process in tight-oil reservoirs and field-pilot designs.

Nomenclature

- c_f = isothermal coefficient of rock compressibility, 1/bar
 D = diffusion coefficient, m²/s
 k = permeability, md [μ d], [nd], [m²]
 k_1 = constant for Eq. C-3, defined in Appendix C, 1/day
 L = core-plug length, m
 N_{Pe} = Péclet number, dimensionless
 P = pressure, bar
 t = time, hours [seconds], [day]
 T = temperature, °C
 u = Darcy velocity, m/s
 V = volume, cm³ [m³]
 z = height of the oil column in the cell in bulk-phase tests, cm
 μ = viscosity, Pa·s
 ρ = density, kg/cm³
 ϕ = porosity, % bulk volume
 $\frac{\partial p}{\partial t}$ = pressure drop, Pa/s

Subscripts

- atm = atmosphere
eff = effective
eq = equilibrium
 f = final
 g = gas
 gc = critical gas
 i = initial
 o = oil
sat = saturation
set = setting conditions

Acknowledgments

We are grateful to the Canada First Research Excellence Fund through the University of Alberta, Future Energy Systems under Project T07-P05 for their financial support.

References

- Aguilera, R. and Vargas, J. F. R. 2016. Factors Controlling Fluid Migration and Distribution in the Eagle Ford Shale. *SPE Res Eval & Eng* **19** (3): 403–414. SPE-171626-PA. <https://doi.org/10.2118/171626-PA>.
- Alharthy, N., Teklu, T. W., Kazemi, H. et al. 2018. Enhanced Oil Recovery in Liquid-Rich Shale Reservoirs: Laboratory To Field. *SPE Res Eval & Eng* **21** (1): 137–159. SPE-175034-PA. <https://doi.org/10.2118/175034-PA>.
- Baek, S. and Akkutlu, I. Y. 2019. Produced-Fluid Composition Redistribution in Source Rocks for Hydrocarbon-In-Place and Thermodynamic Recovery Calculations. *SPE J.* **24** (3): 1395–1414. SPE-195578-PA. <https://doi.org/10.2118/195578-PA>.
- Bear, J. 2013. *Dynamics of Fluids in Porous Media*. Chelmsford, Massachusetts, USA: Courier Corporations.
- Birdsell, D. T., Karra, S., and Rajaram, H. 2018. On the Representation of the Porosity-Pressure Relationship in General Subsurface Flow Codes. *Water Resour Res* **54** (2): 1382–1388. <https://doi.org/10.1002/2017WR022001>.
- Bradley, P. S. and Mangasarian, O. L. 2000. k-Plane Clustering. *J Global Optim* **16** (1): 23–32. <https://doi.org/10.1023/A:1008324625522>.
- Bui, K. and Akkutlu, I. Y. 2017. Hydrocarbons Recovery from Model-Kerogen Nanopores. *SPE J.* **22** (3): 9. SPE-185162-PA. <https://doi.org/10.2118/185162-PA>.
- Calsep A/S. 2018. *PVTsim Nova*, Revision 3. Lyngby, Denmark: Calsep A/S.
- Canada Energy Regulator. 2013. The Ultimate Potential for Unconventional Petroleum from the Montney Formation of British Columbia and Alberta—Energy Briefing Note, <https://www.cer-rec.gc.ca/nrg/sttstc/ntrlgs/rprt/lmtptnlmtnyfrmntn2013/lmtptnlmtnyfrmntn2013-eng.html> (accessed 1 January 2020).
- Carlsen, M., Whitson, C., Dahouk, M. M. et al. 2019. Compositional Tracking of a Huff-n-Puff Project in the Eagle Ford. Paper presented at the SPE/AAPG/SEG Unconventional Resources Technology Conference, Denver, Colorado, USA, 22–24 July. URTEC-2019-539-MS. <https://doi.org/10.15530/urtec-2019-539>.
- Carpenter, C. 2018. A Review of Improved-Oil-Recovery Methods in North American Unconventional Reservoirs. *J Pet Technol* **70** (1): 42–44. SPE-0118-0042-JPT. <https://doi.org/10.2118/0118-0042-JPT>.

- Charbeneau, R. J. 2006. *Groundwater Hydraulics and Pollutant Transport*. Long Grove, Illinois, USA: Waveland Press.
- Chen, C., Balhoff, M. T., and Mohanty, K. K. 2014. Effect of Reservoir Heterogeneity on Primary Recovery and CO₂ Huff 'n' Puff Recovery in Shale Oil Reservoirs. *SPE Res Eval & Eng* **17** (3): 404–413. SPE-164553-PA. <https://doi.org/10.2118/164553-PA>.
- Chen, C. and Gu, M. 2017. Investigation of Cyclic CO₂ Huff-and-Puff Recovery in Shale Oil Reservoirs Using Reservoir Simulation and Sensitivity Analysis. *Fuel* **188**: 102–111. <https://doi.org/10.1016/j.fuel.2016.10.006>.
- Cronin, M., Emani-Meybodi, H., and Johns, R. T. 2019. Diffusion-Dominated Proxy Model for Solvent Injection in Ultratight Oil Reservoirs. *SPE J.* **24** (2): 660–680. SPE-190305-PA. <https://doi.org/10.2118/190305-PA>.
- Davudov, D. and Moghanloo, R. G. 2018. Impact of Pore Compressibility and Connectivity Loss on Shale Permeability. *Int J Coal Geol* **187**: 98–113. <https://doi.org/10.1016/j.coal.2018.01.008>.
- EIA. 2019. Annual Energy Outlook 2019 with Projections to 2050, <https://www.eia.gov/outlooks/aeo/pdf/aeo2019.pdf> (accessed January 2019).
- Fu, Q., Cudjoe, S., Barati, R. et al. 2019. Experimental and Numerical Investigation of the Diffusion-Based Huff-n-Puff Gas Injection into Lower Eagle Ford Shale Samples. Paper presented at the SPE/AAPG/SEG Unconventional Resources Technology Conference, Denver, Colorado, USA, 22–24 July. URTEC-2019-402-MS. <https://doi.org/10.15530/urtec-2019-402>.
- Geoscience BC. 2011. Deep Subsurface Aquifer Characterization in Support of Montney Tight Gas Development: Geological Report, http://cdn.geosciencebc.com/project_data/GBC_Report2011-11/GBC2011-11_Montney_Aquifer_Characterization_Report.pdf (accessed February 2020).
- Ghanizadeh, A., Bhowmik, S., Haeri-Ardakani, O. et al. 2015. A Comparison of Shale Permeability Coefficients Derived Using Multiple Non-Steady-State Measurement Techniques: Examples from the Duvernay Formation, Alberta (Canada). *Fuel* **140**: 371–387. <https://doi.org/10.1016/j.fuel.2014.09.073>.
- Gherabati, S. A., Browning, J., Male, F. et al. 2017. Evaluating Hydrocarbon-in-Place and Recovery Factor in a Hybrid Petroleum System: Case of Bakken and Three Forks in North Dakota. Paper presented at the SPE/AAPG/SEG Unconventional Resources Technology Conference, Austin, Texas, USA, 24–26 July. URTEC-2017-2671498-MS. <https://doi.org/10.15530/URTEC-2017-2671498>.
- Habibi, A., Yassin, M. R., Dehghanpour, H. et al. 2017. Experimental Investigation of CO₂-Oil Interactions in Tight Rocks: A Montney Case Study. *Fuel* **203**: 853–867. <https://doi.org/10.1016/j.fuel.2017.04.077>.
- Hawthorne, S. B., Gorecki, C. D., Sorensen, J. A. et al. 2013. Hydrocarbon Mobilization Mechanisms from Upper, Middle, and Lower Bakken Reservoir Rocks Exposed to CO₂. Paper presented at the SPE Unconventional Resources Conference Canada, Calgary, Alberta, Canada, 5–7 November. SPE-167200-MS. <https://doi.org/10.2118/167200-MS>.
- Hertel, S. A., Rydz, M., Anger, B. et al. 2018. Upscaling of Digital Rock Porosities by Correlation with Whole-Core CT-Scan Histograms. *Petrophysics* **59** (5): 694–702. SPWLA-2018-v59n5a8. <https://www.doi.org/10.30632/PJV59N5-2018a8>.
- Hobbs, B. and Ord, A. 2015. *Structural Geology: The Mechanics of Deforming Metamorphic Rocks*. Amsterdam, The Netherlands: Elsevier. <https://doi.org/10.1016/C2012-0-01215-X>.
- Hoffman, B. T. and Evans, J. G. 2016. Improved Oil Recovery IOR Pilot Projects in the Bakken Formation. Paper presented at the SPE Low Perm Symposium, Denver, Colorado, USA, 5–6 May. SPE-180270-MS. <https://doi.org/10.2118/180270-MS>.
- Hoteit, H. and Firoozabadi, A. 2009. Numerical Modeling of Diffusion in Fractured Media for Gas-Injection and -Recycling Schemes. *SPE J.* **14** (2): 323–337. SPE-103292-PA. <https://doi.org/10.2118/103292-PA>.
- Hughes, J. D. 2013. A Reality Check on the Shale Revolution. *Nature* **494** (7437): 307–308. <https://doi.org/10.1038/494307a>.
- Jacobs, T. 2019. Shale EOR Delivers, So Why Won't the Sector Go Big? *J Pet Technol* **71** (5): 37–41. SPE-0519-0037-JPT. <https://doi.org/10.2118/0519-0037-JPT>.
- Javadpour, F. 2009. Nanopores and Apparent Permeability of Gas Flow in Mudrocks (Shales and Siltstone). *J Can Pet Technol* **48** (8): 16–21. PETSOC-09-08-16-DA. <https://doi.org/10.2118/09-08-16-DA>.
- Jin, L., Hawthorne, S., Sorensen, J. et al. 2017. Utilization of Produced Gas for Improved Oil Recovery and Reduced Emissions from the Bakken Formation. Paper presented at the SPE Health, Safety, Security, Environment, & Social Responsibility Conference—North America, New Orleans, Louisiana, USA, 18–20 April. SPE-184414-MS. <https://doi.org/10.2118/184414-MS>.
- King, G. 2014. Maximizing Recovery Factors: Improving Recovery Factors in Liquids-Rich Resource Plays Requires New Approaches. *The American Oil and Gas Reporter*, <https://www.aogr.com/magazine/editors-choice/improving-recovery-factors-in-liquids-rich-resource-plays-requires-new-appr> (accessed December 2019).
- Kurtoglu, B. 2013. *Integrated Reservoir Characterization and Modeling in Support of Enhanced Oil Recovery for Bakken*. PhD dissertation. Colorado School of Mines, Golden, Colorado, USA. <http://hdl.handle.net/11124/24>.
- Lan, Y., Moghanloo, R. G., and Davudov, D. 2017. Pore Compressibility of Shale Formations. *SPE J.* **22** (6): 1778–1789. SPE-185059-PA. <https://doi.org/10.2118/185059-PA>.
- Lashgari, H. R., Sun, A., Zhang, T. et al. 2019. Evaluation of Carbon Dioxide Storage and Miscible Gas EOR in Shale Oil Reservoirs. *Fuel* **241**: 1223–1235. <https://doi.org/10.1016/j.fuel.2018.11.076>.
- Leung, J. Y. and Srinivasan, S. 2011. Analysis of Uncertainty Introduced by Scaleup of Reservoir Attributes and Flow Response in Heterogeneous Reservoirs. *SPE J.* **16** (3): 713–724. SPE-145678-PA. <https://doi.org/10.2118/145678-PA>.
- Li, C., Pu, H., Zhong, X. et al. 2020. Interfacial Interactions between Bakken Crude Oil and Injected Gases at Reservoir Temperature: A Molecular Dynamics Simulation Study. *Fuel* **276**: 118058. <https://doi.org/10.1016/j.fuel.2020.118058>.
- Li, D. and Lake, L. W. 1995. Scaling Fluid Flow through Heterogeneous Permeable Media. *SPE Adv Technol Ser* **3** (1): 188–197. SPE-26648-PA. <https://doi.org/10.2118/26648-PA>.
- Li, L. and Sheng, J. J. 2017. Upscale Methodology for Gas Huff-n-Puff Process in Shale Oil Reservoirs. *J Pet Sci Eng* **153**: 36–46. <https://doi.org/10.1016/j.petrol.2017.03.028>.
- Li, S., Qiao, C., Zhang, C. et al. 2018. Determination of Diffusion Coefficients of Supercritical CO₂ Under Tight Oil Reservoir Conditions with Pressure-Decay Method. *J CO₂ Util* **24**: 430–443. <https://doi.org/10.1016/j.jcou.2018.02.002>.
- Liu, D., Yuan, P., Liu, H. et al. 2013. High-Pressure Adsorption of Methane on Montmorillonite, Kaolinite and Illite. *Appl Clay Sci* **85**: 25–30. <https://doi.org/10.1016/j.clay.2013.09.009>.
- Lou, X., Chakraborty, N., Karpyn, Z. et al. 2019. Experimental Study of Gas-Liquid Diffusion in Porous Rocks and Bulk Fluids To Investigate the Effect of Rock Matrix Hindrance. Paper presented at the SPE Annual Technical Conference and Exhibition, Calgary, Alberta, Canada, 30 September–2 October. SPE-195941-MS. <https://doi.org/10.2118/195941-MS>.
- Ma, Y. Z. and Holditch, S. A. 2015. *Unconventional Oil and Gas Resources Handbook*, first edition. Houston, Texas, USA: Gulf Professional Publishing.
- McGuire, P. L., Okuno, R., Gould, T. L. et al. 2017. Ethane-Based Enhanced Oil Recovery: An Innovative and Profitable Enhanced-Oil-Recovery Opportunity for a Low-Price Environment. *SPE Res Eval & Eng* **20** (1): 42–58. SPE-179565-PA. <https://doi.org/10.2118/179565-PA>.
- McPhee, C., Reed, J., and Zubizarreta, I. 2015. *Core Analysis: A Best Practice Guide*, first edition, Vol. 64, Chap. 4. Amsterdam, The Netherlands: Elsevier.

- Moulu, J. C. 1989. Solution-Gas Drive: Experiments and Simulation. *J Pet Sci Eng* **2** (4): 379–386. [https://doi.org/10.1016/0920-4105\(89\)90011-9](https://doi.org/10.1016/0920-4105(89)90011-9).
- Nelson, P. H. 2009. Pore-Throat Sizes in Sandstones, Tight Sandstones, and Shales. *AAPG Bull* **93** (3): 329–340. <https://doi.org/10.1306/10240808059>.
- NIST. 2018. *Thermochemical Properties of Fluid Systems*. Washington, DC, USA: US Department of Commerce. <http://webbook.nist.gov/chemistry>.
- Olorede, O. M., Akkutlu, I. Y., and Efendiev, Y. 2017. Compositional Reservoir-Flow Simulation for Organic-Rich Gas Shale. *SPE J.* **22** (6): 1963–1983. SPE-182667-PA. <https://doi.org/10.2118/182667-PA>.
- Orozco, D., Fragoso, A., Selvan, K. et al. 2020. Eagle Ford Huff ‘n’ Puff Gas-Injection Pilot: Comparison of Reservoir-Simulation, Material Balance and Real Performance of the Pilot Well. *SPE Res Eval & Eng* **23** (1): 247–260. SPE-191575-PA. <https://doi.org/10.2118/191575-PA>.
- Ozkan, E., Raghavan, R. S., and Apaydin, O. G. 2010. Modeling of Fluid Transfer from Shale Matrix to Fracture Network. Paper presented at the SPE Annual Technical Conference and Exhibition, Florence, Italy, 19–22 September. SPE-134830-MS. <https://doi.org/10.2118/134830-MS>.
- Pacheco-Roman, F. J. and Hejazi, S. H. 2015. Estimation of Solubility and Diffusivity of Gases in Heavy Oils by Use of Late-Time Pressure-Decay Data: An Analytical/Graphical Approach. *SPE J.* **20** (4): 717–728. SPE-170957-PA. <https://doi.org/10.2118/170957-PA>.
- Peng, D. Y. and Robinson, D. B. 1978. *The Characterization of the Heptanes and Heavier Fractions for the GPA Peng-Robinson Programs*. GPA Research Report RR-28, Gas Producers Association, Tulsa, Oklahoma, USA.
- Perkins, T. K. and Johnston, O. C. 1963. A Review of Diffusion and Dispersion in Porous Media. *SPE J.* **3** (1): 70–84. SPE-480-PA. <https://doi.org/10.2118/480-PA>.
- Rasmussen, M. L. and Civan, F. 2009. Parameters of Gas Dissolution in Liquids Obtained by Isothermal Pressure Decay. *AIChE J* **55** (1): 9–23. <https://doi.org/10.1002/aic.11669>.
- Rassenfoss, S. 2017. Shale EOR Works, but Will It Make a Difference? *J Pet Technol* **69** (10): 34–40. SPE-1017-0034-JPT. <https://doi.org/10.2118/1017-0034-JPT>.
- Reynolds, M., Bachman, R., Buendia, J. et al. 2015. The Full Montney—A Critical Review of Well Performance by Production Analysis of Over 2,000 Montney Multi-Stage Fractured Horizontal Gas Wells. Paper presented at the SPE/CSUR Unconventional Resources Conference, Calgary, Alberta, Canada, 20–22 October. SPE-175948-MS. <https://doi.org/10.2118/175948-MS>.
- Sadrzadeh, M., Amirilargani, M., Shahidi, K. et al. 2011. Pure and Mixed Gas Permeation through a Composite Polydimethylsiloxane Membrane. *Polym Adv Technol* **22** (5): 586–597. <https://doi.org/10.1002/pat.1551>.
- Sanchez-Rivera, D., Mohanty, K., and Balhoff, M. 2015. Reservoir Simulation and Optimization of Huff-and-Puff Operations in the Bakken Shale. *Fuel* **147**: 82–94. <https://doi.org/10.1016/j.fuel.2014.12.062>.
- Sing, K. S. W., Everett, D. H., Haul, R. A. W. et al. 1985. Reporting Physisorption Data for Gas/Solid Systems with Special Reference to the Determination of Surface Area and Porosity. *Pure Appl Chem* **57** (4): 603–619. <https://doi.org/10.1351/pac198557040603>.
- Song, C. and Yang, D. 2017. Experimental and Numerical Evaluation of CO₂ Huff-n-Puff Processes in Bakken Formation. *Fuel* **190**: 145–162. <https://doi.org/10.1016/j.fuel.2016.11.041>.
- Thakur, G. 2019. Enhanced Recovery Technologies for Unconventional Oil Reservoirs. *J Pet Technol* **71** (9): 66–69. SPE-0919-0066-JPT. <https://doi.org/10.2118/0919-0066-JPT>.
- Tran, S., Eghbali, S., and Dehghanpour, H. 2020. Studying Phase Behavior of Oil/Natural-Gas Systems for Designing Gas Injection Operations: A Montney Case Study. *SPE Res Eval & Eng* **23** (3): 943–961. SPE-201109-PA. <https://doi.org/10.2118/201109-PA>.
- Wood, D. J., Lake, L. W., Johns, R. T. et al. 2008. A Screening Model for CO₂ Flooding and Storage in Gulf Coast Reservoirs Based on Dimensionless Groups. *SPE Res Eval & Eng* **11** (3): 513–520. SPE-100021-PA. <https://doi.org/10.2118/100021-PA>.
- Yassin, M. R. 2019. *Evaluation of Wettability and EOR Potential of Shale and Tight Formations*. PhD dissertation, University of Alberta, Edmonton, Alberta, Canada. <https://doi.org/10.7939/r3-t4p7-v554>.
- Yassin, M. R., Habibi, A., Zolfaghari, A. et al. 2018. An Experimental Study of Nonequilibrium Carbon Dioxide/Oil Interactions. *SPE J.* **23** (5): 1768–1783. SPE-187093-PA. <https://doi.org/10.2118/187093-PA>.
- Yu, W., Lashgari, H. R., Wu, K. et al. 2015. CO₂ Injection for Enhanced Oil Recovery in Bakken Tight Oil Reservoirs. *Fuel* **159**: 354–363. <https://doi.org/10.1016/j.fuel.2015.06.092>.
- Yu, Y., Li, L., and Sheng, J. J. 2017. A Comparative Experimental Study of Gas Injection in Shale Plugs by Flooding and Huff-n-Puff Processes. *J Nat Gas Sci Eng* **38**: 195–202. <https://doi.org/10.1016/j.jngse.2016.12.040>.
- Zhang, Y. P., Hyndman, C. L., and Maini, B. B. 2000. Measurement of Gas Diffusivity in Heavy Oils. *J Pet Sci Eng* **25** (1–2): 37–47. [https://doi.org/10.1016/S0920-4105\(99\)00031-5](https://doi.org/10.1016/S0920-4105(99)00031-5).
- Zick, A. A. 1986. A Combined Condensing/Vaporizing Mechanism in the Displacement of Oil by Enriched Gases. Paper presented at the SPE Annual Technical Conference and Exhibition, New Orleans, Louisiana, USA, 5–8 October. SPE-15493-MS. <https://doi.org/10.2118/15493-MS>.

Appendix A—Images of Interactions at the Gas/Oil Interface in Bulk-Phase Tests (Tran et al. 2020)

Bulk phase visualization tests are shown in Fig. A-1. Details of experimental conditions and results for oil/C₁ and oil/C₁/C₂ tests are shown in Fig. A-2. In Fig. A-2, volume expansion factor (VEF) of the oil caused by the dissolution of injected gas is

$$\text{VEF} = \frac{(V_o)_{P, T_{\text{set}}}}{(V_i)_{P_{\text{atm}}, T_{\text{set}}}}, \quad \dots \quad (\text{A-1})$$

where V_o is the oil volume at a pressure P and T_{set} divided by the initial oil volume V_i at P_{atm} and T_{set} . Because C₂ is more soluble in oil than C₁ at the same P and T , the presence of C₂ in the injected gas enhances oil swelling compared with the C₁ case (comparing the VEF at equilibrium condition in oil/C₁ and oil/C₁/C₂ tests).

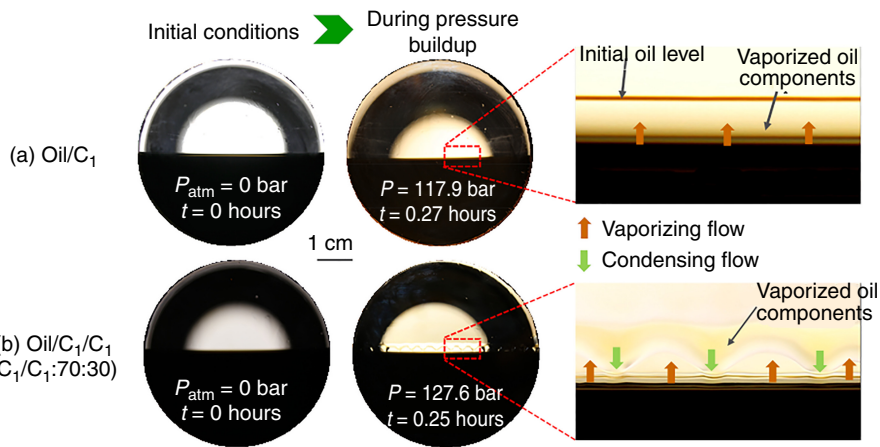


Fig. A-1—Images captured at the gas/oil interface during the pressure buildup process: (a) vaporizing flows in the oil/C₁ test, and (b) vaporizing and condensing flows in the oil/C₁/C₂ (C₁/C₂:70:30 mol%) test at 50°C.

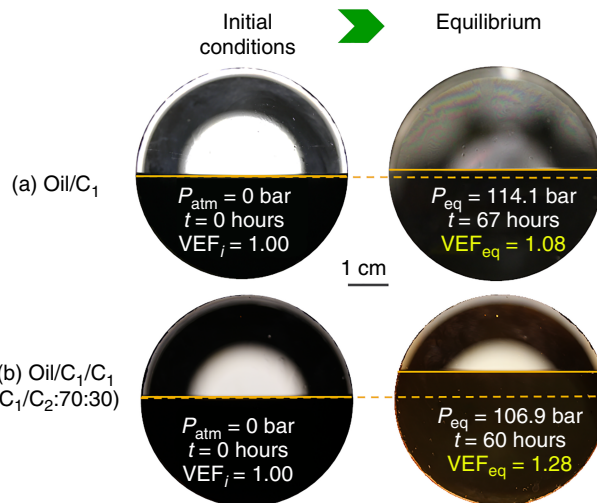


Fig. A-2—Images of gas/oil interface at initial and equilibrium conditions in (a) oil/C₁, and (b) oil/C₁/C₂ (C₁/C₂:70:30 mol%) tests. The temperature was kept at 50°C during the experiment.

Appendix B—Supplementary Material

Supplementary material to this manuscript can be found online at <https://drive.google.com/file/d/1HRrTbDwe3hCbsFilkcJKXa-doAU8o8Q1N/view?usp=sharing>.

Appendix C—Pressure-Decline Region Classification by Data Clustering Method and Péclet Number Calculations

Fig. C-1 shows pressure-decline regions classified by the *k*-plane clustering method. **Fig. C-2** shows the *N_{Pe}* profiles during the soaking period.

To evaluate the relative importance of advection vs. diffusion, we calculate the dimensionless *N_{Pe}* (Hobbs and Ord 2015) by

$$N_{Pe} = \frac{u \times L}{D_{eff}}, \quad \dots \dots \dots \quad (C-1)$$

where, *u*, *L*, and *D_{eff}* are Darcy velocity, length of the core plug, and effective diffusion coefficient, respectively. *D_{eff}* (Li et al. 2018) is calculated by

$$D_{eff} = \phi \times D, \quad \dots \dots \dots \quad (C-2)$$

where ϕ and *D* are porosity and bulk-phase diffusion coefficient, respectively. *D* can be estimated using an analytical model proposed by Zhang et al. (2000):

$$D = -\frac{4z_o^2 \times k_1}{\pi^2}, \quad \dots \dots \dots \quad (C-3)$$

where *z_o* and *k₁* are the height of the oil column in the cell and a constant determined by regression of the pressure-time relations for bulk-phase tests (oil/C₁ and oil/C₁/C₂ systems in Fig. 5b), respectively. It should be noted that only one *D* value is derived from each bulk-phase test.

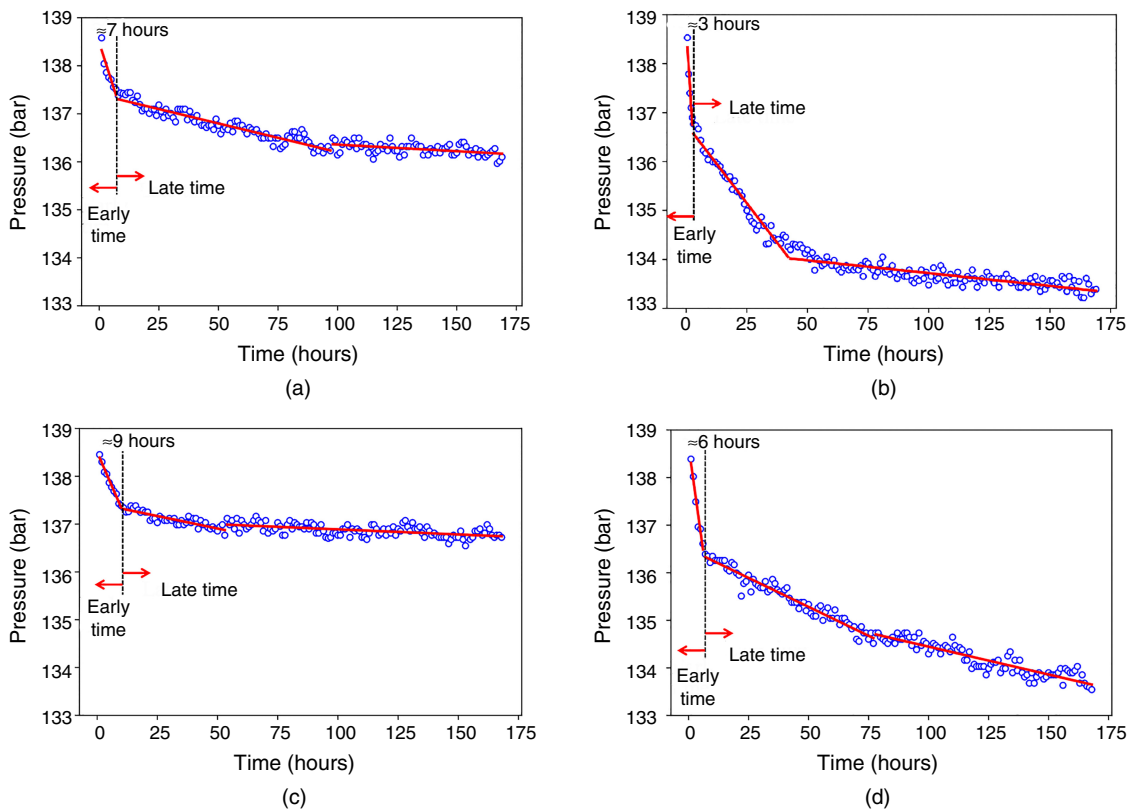


Fig. C-1—Pressure-decline regions classification by k -plane clustering method: (a) Set 1-C₁, (b) Set 1-C₁/C₂, (c) Set 2-C₁, and (d) Set 2-C₁/C₂.

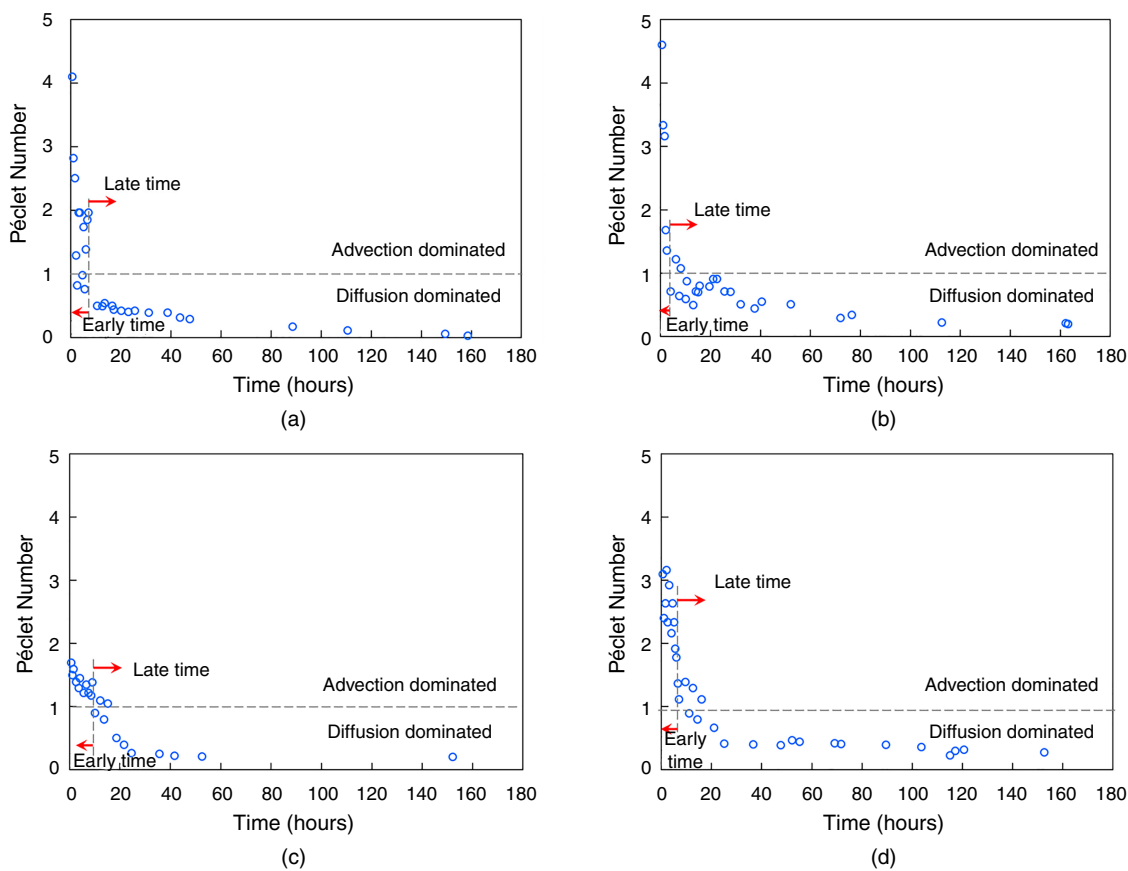


Fig. C-2— N_{Pe} profiles during soaking period: (a) Set 1-C₁, (b) Set 1-C₁/C₂, (c) Set 2-C₁, and (d) Set 2-C₁/C₂.

Darcy velocity u is calculated as

Also, the continuity equation (Charbeneau 2006; Bear 2013; Birdsall et al. 2018) can be written as

As an approximation, we assume that u is constant along the plug. This results in $\frac{\partial u}{\partial x} = 0$. Therefore, Eq. C-5 can be written as

where $\frac{\partial p}{\partial t}$ is calculated for the two pressure-decline regions, early and late times of the four HnP tests, as shown in Fig. C-1.

Finally, by combining Eqs. C-1 through C-6, we arrive at the following equation for N_{Pe} :

$$N_{\text{Pe}} = \frac{\sqrt{-\frac{k}{\mu} \times \frac{\partial p}{\partial t}} \times L}{\phi \times D} \quad \dots \dots \dots \quad (\text{C-7})$$